



Cite this: *Phys. Chem. Chem. Phys.*,
2018, 20, 15344

Aromatic cage-like B_{34} and B_{35}^+ : new axially chiral members of the borospherene family†

Hui Liu,^a Qiang Chen,^{ab} Hai-Ru Li,^a Xiao-Yun Zhao,^a Xin-Xin Tian,^a
Yue-Wen Mu,^{id} ^a Hai-Gang Lu^a and Si-Dian Li^{id} *^a

Shortly after the discovery of all-boron fullerenes $D_{2d} B_{40}^{-/0}$ (borospherenes), the first axially chiral borospherenes $C_3/C_2 B_{39}^-$ were characterized in experiments in 2015. Based on extensive global minimum searches and first-principles theory calculations, we present herein two new axially chiral members to the borospherene family: the aromatic cage-like $C_2 B_{34}$ (**1**) and $C_2 B_{35}^+$ (**2**). Both B_{34} (**1**) and B_{35}^+ (**2**) feature one B_{21} boron triple chain on the waist and two equivalent heptagons and hexagons on the cage surface, with the latter being obtained by the addition of B^+ into the former at the tetracoordinate defect site. Detailed bonding analyses show that they follow the universal bonding pattern of $\sigma + \pi$ double delocalization, with 11 delocalized π bonds over a σ skeleton. Extensive molecular dynamics simulations show that these borospherenes are kinetically stable below 1000 K and start to fluctuate at 1200 K and 1100 K, respectively. The IR, Raman, and UV-vis spectra of **1** and **2** are computationally simulated to facilitate their experimental characterization.

Received 19th March 2018,
Accepted 3rd May 2018

DOI: 10.1039/c8cp01769g

rsc.li/pccp

1. Introduction

Six years after the discovery of C_{60} and C_{70} ,¹ the first axially chiral fullerene C_{76} was characterized in experiments in 1991,² arousing considerable attention to the chirality of atomic clusters. As the light neighbor of carbon in the periodic table, boron shares with carbon the rare ability to form stable covalently bonded molecular frameworks by bonding to itself. However, as a prototypical electron-deficient element, boron exhibits strong propensity to form multicenter two-electron (mc-2e) bonds in both bulk allotropes and polyhedral compounds. The possibility of all-boron fullerenes was not considered for over two decades before Yakobson and coworkers proposed a perfect buckyball B_{80} in 2007 by capping the twenty hexagons of C_{60} .³ However, subsequent global minimum searches and density functional theory (DFT) calculations at various theoretical levels indicate that such a B_{80} cage is much less stable than its core-shell type counterparts in thermodynamics.⁴

Persistent joint photoelectron spectroscopy (PES) and first-principles theory investigations in the past decade have confirmed that small $B_n^{-/0}$ possess planar or quasi-planar (2D) structures in an unexpectedly wide range of cluster size ($n = 3-30, 33-38$),⁵⁻¹⁴

including the chiral quasi-planar $C_1 B_{30}^-$ and $C_1 B_{34}^-$,^{10,11} unveiling a flat world of boron in close analogy to planar aromatic hydrocarbons with unique fluxional behavior.^{15,16} The first cage-like all-boron fullerenes $D_{2d} B_{40}^{-/0}$, dubbed borospherenes, were discovered in 2014 in a joint PES and theoretical investigation.¹⁷ The fluxional and aromatic behavior of B_{40} as a nanobubble is discussed in detail in ref. 18. Endohedral metallo-borospherenes $M@B_{40}$ ($M = Ca, Sr$) and noble gas encapsulated $Ng@B_{40}$ were later predicted to be viable species.^{19,20} The first axially chiral borospherenes $C_3/C_2 B_{39}^-$ were characterized in PES measurements in 2015.²¹ They were later doped with Ca^{2+} to form endohedral $Ca@B_{39}^+$.²² The borospherene family has been extended in the past three years to include B_{41}^+ , B_{42}^{2+} ,²³ B_{38}^{2-} (in $Ca@B_{38}$), B_{37}^{3-} (in $Ca@B_{37}^-$), and B_{36}^{4-} (in $Li_4@B_{36}$).²⁴⁻²⁶ These B_n^q borospherenes ($n = 36-42$, $q = n - 40$) are all composed of twelve interwoven boron double chains (BDCs) with six hexagonal or heptagonal facets and follow the universal bonding pattern of $\sigma + \pi$ double delocalization with 12 delocalized π bonds over a σ -skeleton. Seashell-like chiral $C_2 B_{28}^{-/0}$ and achiral $C_s B_{29}^-$ borospherenes were recently observed in PES experiments as minor isomers.^{8,9} Cage-like $D_{2h} B_{38}$ and $C_2 B_{44}$ were also reported at various theoretical levels.^{27,28} Ion mobility experiments in combination with DFT calculations indicate that double-ring tubular structures start to occur at B_{16}^+ in B_n^+ monocations ($n = 16-25$).²⁹ Extensive global searches show that cage-like $D_{2d} B_{40}^+$,³⁰ $C_s B_{39}^+$,³¹ and $C_s B_{29}^+$ ³² are the global minima (GM) of the monocations. Doping boron clusters has appeared to be an effective way to induce the formation of unusual topologies in boron clusters including cages.^{33,34}

^a Nanocluster Laboratory, Institute of Molecular Science, Shanxi University, Taiyuan 030006, China. E-mail: ywmu@sxu.edu.cn, luhg@sxu.edu.cn, lisidian@sxu.edu.cn

^b Beijing National Laboratory for Molecular Sciences, State Key Laboratory for Structural Chemistry of Unstable and Stable Species, Institute of Chemistry, Chinese Academy of Sciences, Beijing 100190, China

† Electronic supplementary information (ESI) available. See DOI: 10.1039/c8cp01769g

Extensive GM searches and first-principles theory calculations performed in this work present two new axially chiral members to the borospherene family, including the aromatic cage-like C_2 $B_{34}(1)$ and C_2 $B_{35}^+(2)$ which are well-defined GMs of the systems. Both $B_{34}(1)$ and $B_{35}^+(2)$ feature one B_{21} boron triple-chain (BTC) on the waist and two hexagons and two heptagons on the cage surface and conform to the universal bonding pattern of $\sigma + \pi$ double delocalization. B_{28} , B_{34} , and B_{40} neutrals and B_{29}^+ , B_{35}^+ , and B_{41}^+ monocations thus form two borospherene series with the difference of six boron atoms.

2. Theoretical approaches

Extensive GM structural searches were carried out on B_{34} and B_{35}^+ using both the minima hopping (MH) algorithm^{35,36} and TGmin approach^{37,38} independently, in combination with manual structural constructions based on low-lying planar, tubular and cage-like isomers of $B_{34}^{-/011}$ and $B_{35}^{-/12}$ reported previously. In total, about 6500 and 6000 stationary points were probed for B_{34} and B_{35}^+ , respectively. Full structural optimization and vibrational analyses were then performed at both the DFT-PBE0 and TPSSH^{39,40} levels with an all-electron 6-311+G(d) basis set⁴¹ implemented in the Gaussian 09 suite.⁴² Single point energies of the five lowest-lying isomers were further refined at PBE0 geometries using a more accurate coupled cluster method with triple excitations (CCSD(T))^{43–45} with the 6-31G(d) basis set implemented in MOLPRO.⁴⁶ The obtained GMs C_2 $B_{34}(1)$ and C_2 $B_{35}^+(2)$ and their degenerate enantiomers C_2 $B_{34}(1')$ and C_2 $B_{35}^+(2')$ are shown in Fig. 1. More alternative low-lying isomers are summarized in Fig. S1 and S2 (ESI[†]) for B_{34} and B_{35}^+ , respectively. Nucleus-independent chemical shifts (NICS)⁴⁷ were calculated at

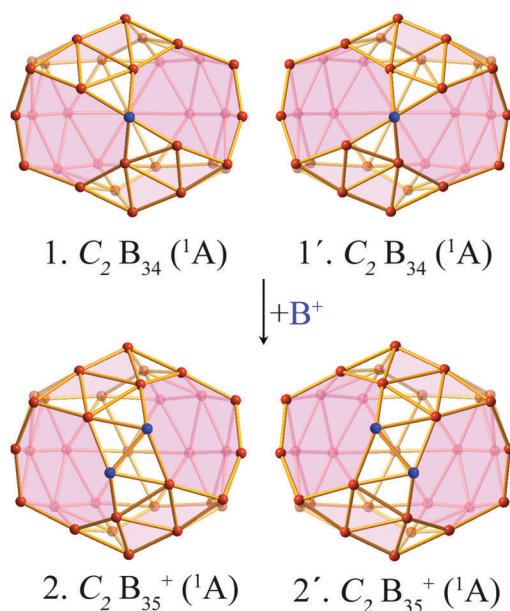


Fig. 1 Optimized structures of the axially chiral borospherenes C_2 $B_{34}(1)$ and C_2 $B_{35}^+(2)$ and their degenerate enantiomers C_2 $B_{34}(1')$ and C_2 $B_{35}^+(2')$, with the B_7 heptagons and B_6 hexagons highlighted in pink and tetra-coordinate boron atom(s) in the front in blue.

the cage centers to assess the spherical aromaticity of $B_{34}(1)$ and $B_{35}^+(2)$. Their chemical bonding patterns were analyzed by employing the adaptive natural density partitioning (AdNDP) method.⁴⁸ Extensive Born–Oppenheimer molecular dynamics simulations were performed for C_2 $B_{34}(1)$ and C_2 $B_{35}^+(2)$ at 1000 K, 1100 K, and 1200 K for 30 ps using the CP2K software.⁴⁹

3. Results and discussion

3.1 Structures and stabilities

As shown in the configurational energy spectrum of B_{34} at the PBE0 level in Fig. 2a, the axially chiral cage-like C_2 $B_{34}(1)$ is the GM of neutral B_{34} with the lowest vibrational frequency of 129 cm^{-1} . It consists of forty-six triangles and four polygonal holes, including two equivalent neighboring B_7 heptagons on the waist and two equivalent separated B_6 hexagons on the top and bottom, with an unusual tetracoordinate B atom highlighted in blue in the front as the defect site (Fig. 1). $B_{34}(1)$ possesses a B_{21} boron triple-chain (BTC) on the waist at the back which is one half of the previously reported triple-ring tubular B_{42} .⁵⁰ It follows Euler's rule for a polyhedron, which in this case reads: E (82 edges) = F (46 triangular + 2 hexagonal + 2 heptagonal faces) + V (34 vertices) – 2. The second lowest-lying cage-like C_s B_{34} with forty-nine boron triangles, two B_6 hexagons, and one B_9 nonagon on the surface lies 0.10 eV higher than the C_2 GM at PBE0 (Fig. 2a). The energy difference is increased to 0.24 eV at a more accurate CCSD(T) level, indicating that C_2 $B_{34}(1)$ is the well-defined GM of the system. We also notice that most of the low-lying B_{34} isomers are cage-like, whereas the first quasi-planar isomer C_1 B_{34} which has the same geometry as the

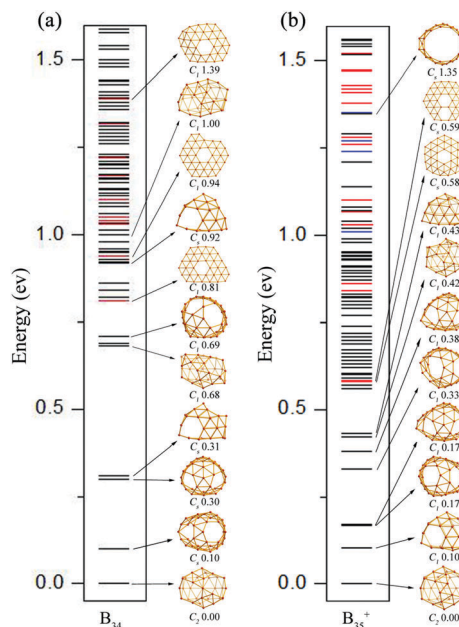


Fig. 2 Configurational energy spectra of (a) B_{34} and (b) B_{35}^+ at the PBE0/6-311+G* level. The energy of the global minimum is taken to be zero and the relative energies are in eV. The black, red, and blue bars denote fullerene-like cages, quasi-planar, and triple-ring tubular structures, respectively.

experimentally observed monoanion B_{34}^- lies much higher (by 0.81 eV) than the cage-like GM at PBE0.

Adding one more B^+ into $B_{34}(1)$ at the tetracoordinate defect site produces the axially chiral cage-like $C_2 B_{35}^+(2)$ which appears to be the GM of the monocation with the lowest vibrational frequency of 154 cm^{-1} (Fig. 1 and Fig. 2b). Similar to $B_{34}(1)$, $B_{35}^+(2)$ also possesses a B_{21} BTC on the waist at the back, with forty-eight triangles, two equivalent B_7 heptagons, and two equivalent B_6 hexagons on the cage surface (Fig. 1) to follow Euler's rule: E (85 edges) = F (48 triangular + 2 hexagonal + 2 heptagonal faces) + V (35 vertices) – 2. From another perspective of view, $B_{35}^+(2)$ can be viewed as a combination of interwoven BDCs and a B_{21} BTC, presenting the first borospherene monocation with a BTC on the waist. As shown in Fig. 2b, there exist seven low-lying cage-like structures within 0.5 eV above the GM. The second lowest-lying isomer $C_1 B_{35}^+$ with one B_5 pentagon, two B_6 hexagons, and one B_7 heptagon on the surface turns out to lie 0.10 eV higher than $B_{35}^+(2)$ at PBE0. This energy difference is improved to 0.15 eV at CCSD(T). It is noticed from Fig. 2b that the planar $C_s B_{35}^+$ with a hexagon at the center, planar $C_s B_{35}^+$ with a double-hexagonal vacancy (which has the same geometry as the experimentally observed B_{35}^{-12}), and the triple-ring tubular $C_s B_{35}^+$ lie 0.58, 0.59, and 1.35 eV higher than $C_2 B_{35}^+(2)$ at PBE0, respectively.

Extensive molecular dynamics (MD) simulations were performed on $B_{34}(1)$ and $B_{35}^+(2)$ to check their dynamical behavior and structural fluctuations at different temperatures. As shown in Fig. 3 and Fig. S3 (ESI[†]), both the borospherenes are dynamically stable at 1000 K, with the average root-mean-square-deviations of RMSD = 0.11 and 0.11 Å and maximum bond length deviations of MAXD = 0.41 and 0.42 Å, respectively. However, further MD simulations indicate that $B_{34}(1)$ and $B_{35}^+(2)$ start to fluctuate at 1200 K and 1100 K with RMSD = 0.16 and 0.21 Å and

MAXD = 0.69 and 1.09 Å, respectively, similar to the situation observed in B_{39}^- , B_{39}^+ , B_{40} , B_{40}^+ , B_{41}^+ and B_{42}^{2+} .^{17,18,21,23,30,31} Detailed analyses indicate that $B_{34}(1)$ and $B_{35}^+(2)$ hop between three and four of their lowest-lying isomers *via* concerted mechanisms mainly involving continuous structural conversions between neighboring hexagons and heptagons (Fig. 3 and Fig. S3, ESI[†]), respectively, similar to the MXW transformation observed in the axially chiral $C_3/C_2 B_{39}^-$ borospherenes.⁵¹

3.2 Bonding analyses

The high thermodynamic and dynamic stabilities of these cage-like clusters originate from their unique bonding patterns. As shown in Fig. 4a, detailed AdNDP analyses indicate that $C_2 B_{34}(1)$ possesses 30 3c-2e σ bonds, 3 5c-2e σ bonds, 6 6c-2e σ bonds, and 1 7c-2e σ bond on the cage surface with the occupation numbers between ON = 1.85–1.97 |e|. Specifically, there exists a unique 5c-2e σ bond around the tetracoordinate defect site which can be approximately viewed as a B 2p lone-pair. The remaining 22 valence electrons form 11 delocalized π bonds over the σ -skeleton, including 1 5c-2e π bond over the tetracoordinate defect site in the front, 6 5c-2e π bonds on the waist, 2 6c-2e π bonds over two B_5 pentagonal pyramids and 2 7c-2e π bonds on the top and bottom with ON = 1.84–1.96 |e|. It is noticed that each hexagon and heptagon in $B_{34}(1)$ is surrounded by four delocalized π bonds, similar to the π bond distribution in $D_{2d} B_{40}$.¹⁷ Such a $\sigma + \pi$ double delocalization bonding pattern renders high stability to $B_{34}(1)$.

$B_{35}^+(2)$ has a similar bonding pattern with $B_{34}(1)$ (Fig. 4b). It possesses 32 3c-2e σ bonds, 2 5c-2e σ bonds, 6 6c-2e σ bonds, and 1 7c-2e σ bond on the cage surface, with the 5c-2e σ bond around the tetracoordinate defect site in $B_{34}(1)$ transferred into two 3c-2e σ bonds in $B_{35}^+(2)$. Over the σ -skeleton, there exist 1 6c-2e π bond in the front, 6 5c-2e π bonds on the waist, and 2

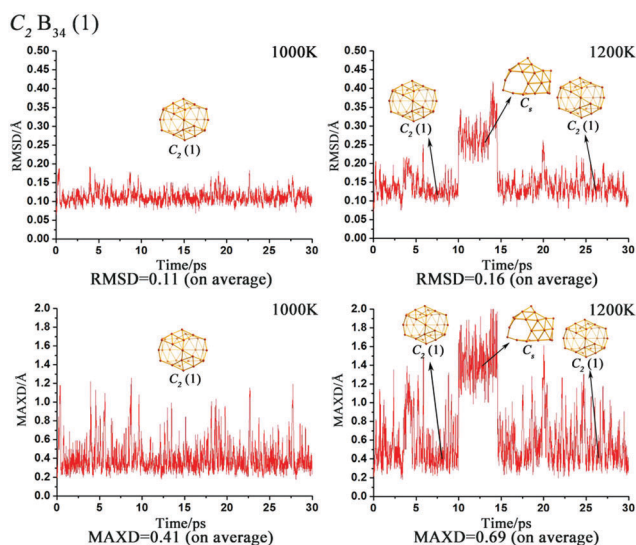


Fig. 3 Born–Oppenheimer molecular dynamics simulations of $C_2 B_{34}(1)$ at 1000 K and 1200 K. The root-mean-square-deviation (RMSD) and maximum bond length deviation (MAXD) values (on average) are indicated in Å.

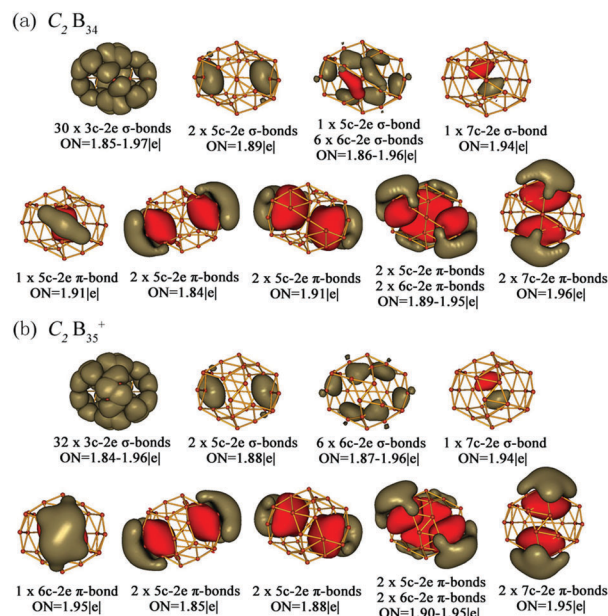


Fig. 4 AdNDP bonding patterns of (a) $C_2 B_{34}(1)$ and (b) $C_2 B_{35}^+(2)$, with the occupation numbers (ONs) indicated.

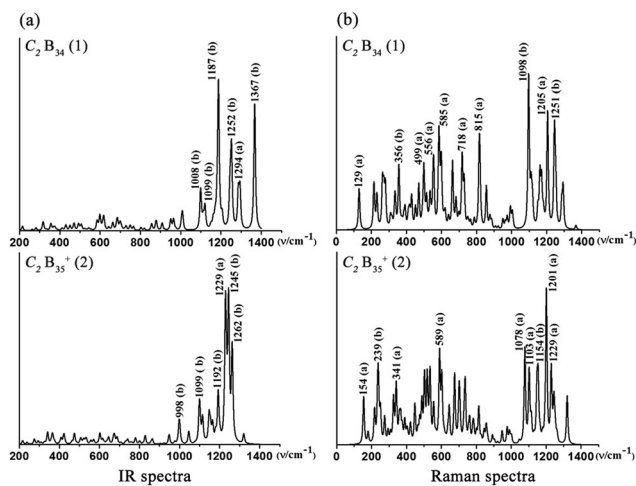


Fig. 5 Simulated IR and Raman spectra of $C_2 B_{34}(1)$ and $C_2 B_{35}^+(2)$ at the TD-PBE0/6-311+G(d) level.

6c-2e π bonds and 2 7c-2e π bonds on the top and bottom. Notably, the 5c-2e π bond over the tetracoordinate defect site in $B_{34}(1)$ is extended to the 6c-2e π bond in $B_{35}^+(2)$ over a B_6 double-chain unit due to the addition of the B^+ monocation. Both $B_{34}(1)$ and $B_{35}^+(2)$ thus possess 11 delocalized π bonds over the σ -skeleton and follow the universal bonding pattern of $\sigma + \pi$ double delocalization. Such a bonding pattern renders three-dimensional aromaticity to both **1** and **2**, as evidenced by the calculated negative NICS values of -40 ppm and -38 ppm at the cage centers at PBE0/6-311+G(d), respectively. These values are well comparable to the corresponding values of -43 , -38 , -41 , and -40 ppm calculated for $D_{2d} B_{40}$, $C_3 B_{39}^-$, $C_1 B_{41}^+$, and $C_2 B_{42}^{2+}$ at the same theoretical level, respectively.^{17,21,23}

3.3 IR, Raman, and UV-vis spectral simulations

Infrared photodissociation (IR-PD) in combination with first-principles theory calculations has proven to be an effective approach in the characterization of novel clusters.^{52,53} $B_{34}(1)$ and $B_{35}^+(2)$ possess 96 (48a + 48b) and 99 (50a + 49b) vibrational modes in total, with 42 and 44 IR active modes and 78 and 83 Raman active modes, respectively. The simulated IR spectra of $B_{34}(1)$ and $B_{35}^+(2)$ calculated at PBE0/6-311+G(d) are shown in Fig. 5a. The two borospherenes appear to have similar IR spectral features with five major IR active peaks at 1008 cm^{-1} (b), 1187 cm^{-1} (b), 1252 cm^{-1} (b), 1294 cm^{-1} (a), and 1367 cm^{-1} (b) in $B_{34}(1)$ and at 1099 cm^{-1} (b), 1192 cm^{-1} (b), 1229 cm^{-1} (b), 1245 cm^{-1} (b), and 1262 cm^{-1} (b) in $B_{35}^+(2)$. All the other IR vibrational modes appear to have much lower intensities.

The simulated Raman spectra of $B_{34}(1)$ and $B_{35}^+(2)$ are shown in Fig. 5b. The major Raman active peaks occur at 129 cm^{-1} (a), 356 cm^{-1} (b), 499 cm^{-1} (a), 556 cm^{-1} (a), 585 cm^{-1} (a), 718 cm^{-1} (a), 815 cm^{-1} (a), 1098 cm^{-1} (b), 1205 cm^{-1} (a), and 1251 cm^{-1} (b) in $B_{34}(1)$ and 154 cm^{-1} (a), 239 cm^{-1} (b), 341 cm^{-1} (a), 589 cm^{-1} (a), 1078 cm^{-1} (a), 1103 cm^{-1} (a), 1154 cm^{-1} (b), 1201 cm^{-1} (a), and 1229 cm^{-1} (a) in $B_{35}^+(2)$. The Raman vibrational modes at 129 cm^{-1} (a) in $B_{34}(1)$ and 154 cm^{-1} (a) in $B_{35}^+(2)$ correspond to the typical ‘‘radial breathing modes’’

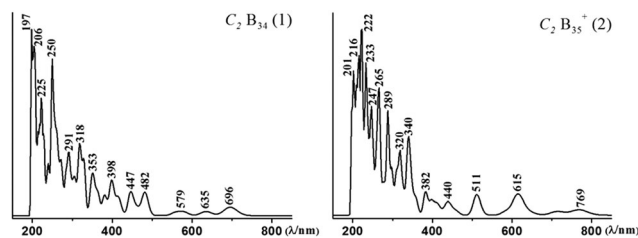


Fig. 6 Simulated UV-vis absorption spectra of $C_2 B_{34}(1)$ and $C_2 B_{35}^+(2)$ at the PBE0/6-311+G(d) level.

(RBMs) of the two borospherenes (Fig. 5). A strong RBM peak at 210 cm^{-1} was used to characterize the hollow structures of single-walled boron nanotubes in experiments.⁵⁴

Finally, we briefly discuss the simulated UV-vis spectra of $B_{34}(1)$ and $B_{35}^+(2)$ using the time-dependent DFT approach⁵⁵ at the PBE0/6-311+G(d) level. The UV spectra of the two species possess similar features, with strong absorption peaks at 197 nm, 225 nm, 250 nm, 291 nm, 318 nm, 353 nm, 398 nm, 447 nm, and 482 nm in $B_{34}(1)$ and 201 nm, 222 nm, 233 nm, 265 nm, 289 nm, 320 nm, 340 nm, 382 nm, 440 nm, 511 nm and 615 nm in $B_{35}^+(2)$. The weak UV-vis absorptions above 600 nm correspond to electronic excitations from the occupied frontier orbitals (HOMO, HOMO-1, and HOMO-2) of the systems (Fig. 6).

4. Conclusions

In summary, we have presented in this work two new axially chiral members $B_{34}(1)$ and $B_{35}^+(2)$ to the borospherene family based on extensive GM searches and first-principles theory calculations. These novel borospherenes feature one B_{21} BTC and four polygons on the cage surface. They are transferable *via* the addition or removal of a B^+ monocation at the tetracoordinate defect site in the front. The two aromatic borospherenes follow the universal bonding pattern of $\sigma + \pi$ double delocalization, with 11 delocalized π bonds over a σ skeleton composed of 40 and 41 delocalized σ bonds, respectively. $B_{34}(1)$ predicted in this work and the experimentally observed B_{28}^8 and B_{40}^{17} form a neutral borospherene series with the difference of six boron atoms, while $B_{35}^+(2)$ and the previously predicted B_{29}^{+32} and B_{41}^{+21} form a similar monocation queue. Future experimental and theoretical investigations are invited to explore the possibility of bigger cage-like borospherenes and viable experimental approaches to synthesize borospherenes or their derivatives in macro-quantities.

Conflicts of interest

There are no conflicts to declare.

Acknowledgements

The project was financially supported by the National Natural Science Foundation of China (21720102006, 21590792, 21373130, 11504213, and 21473106).

Notes and references

- 1 H. W. Kroto, J. R. Heath, S. C. O'Brien, R. F. Curl and R. E. Smalley, *Nature*, 1985, **318**, 162–163.
- 2 R. Ettl, I. Chao, F. Diederich and R. L. Whetten, *Nature*, 1991, **353**, 149–153.
- 3 N. G. Swacki, A. Sadrzadeh and B. I. Yakobson, *Phys. Rev. Lett.*, 2007, **98**, 166804.
- 4 F. Y. Li, P. Jin, D. E. Jiang, L. Wang, S. B. Zhang, J. J. Zhao and Z. F. Chen, *J. Chem. Phys.*, 2012, **136**, 074302.
- 5 A. P. Sergeeva, I. A. Popov, Z. A. Piazza, W. L. Li, C. Romanescu, L. S. Wang and A. I. Boldyrev, *Acc. Chem. Res.*, 2014, **47**, 1349–1358.
- 6 L. S. Wang, *Int. Rev. Phys. Chem.*, 2016, **35**, 69–142.
- 7 X. M. Luo, T. Jian, L. J. Cheng, W. L. Li, Q. Chen, R. Li, H. J. Zhai, S. D. Li, A. I. Boldyrev, J. Li and L. S. Wang, *Chem. Phys. Lett.*, 2017, **683**, 336–341.
- 8 Y. J. Wang, Y. F. Zhao, W. L. Li, T. Jian, Q. Chen, X. R. You, T. Ou, X. Y. Zhao, H. J. Zhai, S. D. Li, J. Li and L. S. Wang, *J. Chem. Phys.*, 2016, **144**, 064307.
- 9 H. R. Li, T. Jian, W. L. Li, Ch. Q. Miao, Y. J. Wang, Q. Chen, X. M. Luo, K. Wang, H. J. Zhai, S. D. Li and L. S. Wang, *Phys. Chem. Chem. Phys.*, 2016, **18**, 29147–29155.
- 10 W. L. Li, Y. F. Zhao, H. S. Hu, J. Li and L. S. Wang, *Angew. Chem., Int. Ed.*, 2014, **53**, 5540–5545.
- 11 Q. Chen, W. L. Li, X. Y. Zhao, H. R. Li, L. Y. Feng, H. J. Zhai, S. D. Li and L. S. Wang, *Eur. J. Inorg. Chem.*, 2017, 4546–4551.
- 12 W. L. Li, Q. Chen, W. J. Tian, H. Bai, Y. F. Zhao, H. S. Hu, J. Li, H. J. Zhai, S. D. Li and L. S. Wang, *J. Am. Chem. Soc.*, 2014, **136**, 12257–12260.
- 13 Z. A. Piazza, H. S. Hu, W. L. Li, Y. F. Zhao, J. Li and L. S. Wang, *Nat. Commun.*, 2014, **5**, 3113.
- 14 Q. Chen, W. J. Tian, L. Y. Feng, H. G. Lu, Y. W. Mu, H. J. Zhai, S. D. Li and L. S. Wang, *Nanoscale*, 2017, **9**, 4550–4557.
- 15 J. O. C. Jimenez-Halla, R. Islas, T. Heine and G. Merino, *Angew. Chem., Int. Ed.*, 2010, **49**, 5668–5671.
- 16 G. Merino and T. Heine, *Angew. Chem., Int. Ed.*, 2012, **51**, 2–4.
- 17 H. J. Zhai, Y. F. Zhao, W. L. Li, Q. Chen, H. Bai, H. S. Hu, Z. A. Piazza, W. J. Tian, H. G. Lu, Y. B. Wu, Y. W. Mu, G. F. Wei, Z. P. Liu, J. Li, S. D. Li and L. S. Wang, *Nat. Chem.*, 2014, **6**, 727–731.
- 18 G. Martínez-Guajardo, J. L. Cabellos, A. Díaz-Celaya, S. Pan, R. Islas, P. K. Chattaraj, T. Heine and G. Merino, *Sci. Rep.*, 2015, **5**, 11287.
- 19 H. Bai, Q. Chen, H. J. Zhai and S. D. Li, *Angew. Chem., Int. Ed.*, 2015, **54**, 941–945.
- 20 S. Pan, M. Ghara, S. Kar, X. Zarate, G. Merino and P. K. Chattaraj, *Phys. Chem. Chem. Phys.*, 2018, **20**, 1953–1963.
- 21 Q. Chen, W. L. Li, Y. F. Zhao, S. Y. Zhang, H. S. Hu, H. Bai, H. R. Li, W. J. Tian, H. G. Lu, H. J. Zhai, S. D. Li, J. Li and L. S. Wang, *ACS Nano*, 2015, **9**, 754–760.
- 22 Q. Chen, T. Gao, W. J. Tian, H. Bai, S. Y. Zhang, H. R. Li, C. Q. Miao, Y. W. Mu, H. G. Lu, H. J. Zhai and S. D. Li, *Phys. Chem. Chem. Phys.*, 2015, **17**, 19690–19694.
- 23 Q. Chen, S. Y. Zhang, H. Bai, W. J. Tian, T. Gao, H. R. Li, C. Q. Miao, Y. W. Mu, H. G. Lu, H. J. Zhai and S. D. Li, *Angew. Chem., Int. Ed.*, 2015, **54**, 8160–8164.
- 24 Q. Chen, H. R. Li, C. Q. Miao, Y. J. Wang, H. G. Lu, Y. W. Mu, G. M. Ren, H. J. Zhai and S. D. Li, *Phys. Chem. Chem. Phys.*, 2016, **18**, 11610–11615.
- 25 Q. Chen, H. R. Li, W. J. Tian, H. G. Lu, H. J. Zhai and S. D. Li, *Phys. Chem. Chem. Phys.*, 2016, **18**, 14186–14190.
- 26 W. J. Tian, Q. Chen, H. R. Li, M. Yan, Y. W. Mu, H. G. Lu, H. J. Zhai and S. D. Li, *Phys. Chem. Chem. Phys.*, 2016, **18**, 9922–9926.
- 27 J. Lv, Y. Wang, L. Zhu and Y. Ma, *Nanoscale*, 2014, **6**, 11692–11696.
- 28 T. B. Tai and M. T. Nguyen, *Chem. Commun.*, 2016, **52**, 1653–1656.
- 29 E. Oger, N. R. M. Crawford, R. Kelting, P. Weis, M. M. Kappes and R. Ahlrichs, *Angew. Chem., Int. Ed.*, 2007, **46**, 8503–8506.
- 30 H. R. Li, Q. Chen, X. X. Tian, H. G. Lu, H. J. Zhai and S. D. Li, *J. Mol. Model.*, 2016, **22**, 124.
- 31 X. Y. Zhao, Q. Chen, H. R. Li, Y. W. Mu, H. G. Lu and S. D. Li, *Phys. Chem. Chem. Phys.*, 2017, **19**, 10998–11003.
- 32 L. Pei, H. R. Li, M. Yan, Q. Chen, Y. W. Mu, H. G. Lu, Y.-B. Wu and S. D. Li, *Phys. Chem. Chem. Phys.*, 2018, DOI: 10.1039/c8cp01078a.
- 33 J. C. Guo, L. Y. Feng, Y. J. Wang, S. Jalife, A. Vásquez-Espinal, J. L. Cabellos, S. Pan, G. Merino and H. J. Zhai, *Angew. Chem., Int. Ed. Engl.*, 2017, **129**, 10308–10311.
- 34 X. Dong, S. Jalife, A. Vásquez-Espinal, E. Ravell, S. Pan, J. L. Cabellos, W. Y. Liang, Z. H. Cui and G. Merino, *Angew. Chem., Int. Ed. Engl.*, 2018, **57**, 4627–4631.
- 35 S. De, A. Willand, M. Amsler, P. Pochet, L. Genovese and S. Goedecker, *Phys. Rev. Lett.*, 2011, **106**, 225502.
- 36 S. Goedecker, W. Hellmann and T. Lenosky, *Phys. Rev. Lett.*, 2005, **95**, 055501.
- 37 X. Chen, Y. F. Zhao, L. S. Wang and J. Li, *Comput. Theor. Chem.*, 2017, **1107**, 57–65.
- 38 Y. F. Zhao, X. Chen and J. Li, *Nano Res.*, 2017, **10**, 3407–3420.
- 39 C. Adamo and V. Barone, *J. Chem. Phys.*, 1999, **110**, 6158–6170.
- 40 J. M. Tao, J. P. Perdew, V. N. Staroverov and G. E. Scuseria, *Phys. Rev. Lett.*, 2003, **91**, 146401.
- 41 R. Krishnan, J. S. Binkley, R. Seeger and J. A. Pople, *J. Chem. Phys.*, 1980, **72**, 650–654.
- 42 M. J. Frisch, *et al.*, *Gaussian 09, Revision A.2*, Gaussian Inc., Wallingford, CT, 2009.
- 43 J. Čížek, *Adv. Chem. Phys.*, 1969, **14**, 35.
- 44 G. D. Purvis and R. J. Bartlett, *J. Chem. Phys.*, 1982, **76**, 1910–1918.
- 45 K. Raghavachari, G. W. Trucks, J. A. Pople and M. HeadGordon, *Chem. Phys. Lett.*, 1989, **157**, 479–483.
- 46 H. J. Werner, P. J. Knowles, G. Knizia, F. R. Manby and M. Schütz, *et al.*, *MOLPRO, version 2012.1*, 2012, <http://www.molpro.net>.
- 47 P. V. R. Schleyer and C. Maerker, *J. Am. Chem. Soc.*, 1996, **118**, 6317–6318.
- 48 D. Y. Zubarev and A. I. Boldyrev, *Phys. Chem. Chem. Phys.*, 2008, **10**, 5207–5217.
- 49 J. VandeVondele, M. Krack, F. Mohamed, M. Parrinello, T. Chassaing and J. Hutter, *Comput. Phys. Commun.*, 2005, **167**, 103–128.

- 50 H. T. Pham, L. V. Duong, N. M. Tam, M. P. Pham-Ho and M. T. Nguyen, *Chem. Phys. Lett.*, 2014, **608**, 295–302.
- 51 T. T. Gao, Q. Chen, Y. W. Mu, H. G. Lu and S. D. Li, *AIP Adv.*, 2016, **6**, 065110.
- 52 G. J. Wang, M. F. Zhou, J. T. Goettel, G. J. Schrobilgen, J. Su, J. Li, T. Schloder and S. Riedel, *Nature*, 2014, **514**, 475–477.
- 53 M. R. Fagiani, X. W. Song, P. Petkov, S. Debnath, S. Gewinner, W. Schöllkopf, T. Heine, A. Felicke and K. R. Asmis, *Angew. Chem., Int. Ed.*, 2017, **56**, 501–504.
- 54 D. Ciuparu, R. F. Klie, Y. M. Zhu and L. Pfefferle, *J. Phys. Chem. B*, 2004, **108**, 3967–3969.
- 55 R. Bauernschmitt and R. Ahlrichs, *Chem. Phys. Lett.*, 1996, **256**, 454–464.